IEEE Access
Multidisciplinary | Rapid Review | Open Access Journal

High-Power and High-Responsivity Avalanche Photodiodes for Self-Heterodyne FMCW Lidar System Applications

Zohauddin Ahmad[1], Yan-Min Liao[1], Sheng-I Kuo[2], You-Chia Chang[2], Rui-Lin Chao[1,2], Naseem[1], Yi-Shan Lee[1], Yung-Jr Hung[3], Huang-Ming Chen[2], Jyehong Chen[2], Jiun-In Guo[4] and Jin-Wei Shi[1*]

[1]Department of Electrical Engineering, National Central University, Jungli, 320, Taiwan
[2]Department of Photonics, National Yang Ming Chiao-Tung University, Hsinchu, 300, Taiwan
[3]Department of Photonics, National Sun Yat-sen University, Kaoshiung, Taiwan
[4]Department of Electronics Engineering, Institute of Electronics, National Yang Ming Chiao-Tung University, Hsinchu, 300, Taiwan

*Corresponding author: Jin-Wei Shi (e-mail: jwshi@ee.ncu.edu.tw).

This work was sponsored by the Ministry of Science and Technology in Taiwan under grants 108-2622-E-008-011-CC2 and 106-2221-E-008 -063 -MY3

ABSTRACT In this work, we demonstrate the high-power and high-responsivity performance of the dual multiplication (M-) layers in $In_{0.52}Al_{0.48}As$ based avalanche photodiode (APD). The dual M-layer design in our APD structure effectively constrains the multiplication process to a thin high-field region rather than the whole thick M-layer. It thus minimizes the space charge effect (SCE) within and avoids increasing the tunneling dark current for the case of directly shrinking M-layer thickness in APD. Furthermore, by combining the specially designed mesa shape with this dual M-layer structure, the edge breakdown can be well suppressed. These benefits lead to an ultra-high gain-bandwidth product (450 GHz; 1 A/W at unit gain) and a high saturation current (>12 mA) can be simultaneously achieved in our device. By nonlinearly driving a wavelength sweeping laser in the self-heterodyne lidar setup, it can generate an optical pulse train-like waveform, providing an effective optical modulation depth of 200% to feed into our demonstrated APD at the receiver-end. Under such scheme, the photo-generated RF (1 GHz) power from our APD with a 6.3 A/W responsivity can be as high as +6.95 dBm at a high (7 mA) output photocurrent. Such high-power and high-responsivity characteristics of our APD can further improve the signal-to-noise (S/N) ratio and dynamic range performances in each pixel of the lidar image. A high-quality 3-dimensional (D) FMCW lidar image is constructed based on our APD, without the integration of any electrical amplifier at the receiver end.

INDEX TERMS Avalanche Photodiodes, FMCW

I. INTRODUCTION

Light detection and ranging (Lidar) technology has become a crucial technology in many different areas including robots, scientific research, remote sensing and medical applications as well as in autonomous vehicle there has been tremendous progress attained over the past few years [1]. For such application, it is necessary to detect in real-time the presence of both fast moving and stationary objects in the surroundings and construct the corresponding 3-D image. The two most used lidar techniques which meet these requirements, involve the pulsed beam (based on the time of flight (ToF) principle) and frequency-modulated continuous wave (FMCW) approaches [2]. Moreover, key features like long-range detection, high spatial resolution, real-time performance, eye safety and interference tolerance are the requisite of the lidar technology. Earlier, engineers preferred using the ToF system due to its simple measurement principles based on direct detection and the simplicity it offered [3]. However, eye safety power restriction limits the maximum ranging distance of a ToF system to around 100 meters [4]. On the other hand, coherent lidar systems based on the FMCW approach, although requires complex digital signal processing (DSP), but it offers excellent resolution with an improved signal-to-noise ratio. This makes them suitable for long range automotive applications which use only coherent light from the coherent laser fed through the local oscillator (LO) for image processing. The incoherent light from solar glare, sunlight or from other lidars in different cars which could cause interference is screened out as in the case of a pulsed lidar. Most FMCW lidar system uses highly linear p-i-n photodiodes (PDs) integrated with a self-heterodyne/homodyne beating setup for high sensitivity and a large saturation current under strong optical LO pumping [5]. In comparison to the p-i-n PD, avalanche photodiodes (APDs) can provide additional multiplication gains and larger signal

to noise (S/N) ratios for the down converted intermediate frequency (IF) signal. However, the extra carrier multiplication process inside the APD slows down the internal carrier transit time, usually resulting in a smaller saturation current than that of the p-i-n PD [6,7], which impeded its application in the self-heterodyne FMCW lidar system. Compared to our previous work [8,9], in this work, we demonstrate the $In_{0.52}Al_{0.48}As$ based vertical-illuminated APD with a novel design in the multiplication region and quadruple mesa shape which can effectively shorten the internal avalanche delay time and suppress the edge breakdown, respectively. As a consequence, a significant reduction in the dark current and higher saturation output photocurrent can be simultaneously achieved. In addition, less bandwidth degradation under a very high operation gain can be attained in our demonstrated APD. The high gain-bandwidth product (450 GHz; 1 A/W unit gain responsivity) and high saturation current (> 12 mA) with high responsivity (6.3 A/W) can be simultaneously achieved in our demonstrated APD. By exciting this device through a wavelength sweeping laser under nonlinear driving in our self-heterodyne lidar setup, we can generate an electrical pulse train providing an effective optical modulation depth of 200%. Such high-power and high-responsivity characteristics of our APD can further improve the signal-to-noise (S/N) ratio and dynamic range performance in each pixel of the lidar image. A high-quality 3-dimensional (D) FMCW lidar image can be constructed using our APD as receiver without the integration of an additional RF low-noise-amplifier (LNA).

II. DEVICE STRUCTURE DESIGN AND FABRICATION

Figures 1 (a) and (b) shows the conceptual cross-sectional view of the APD mesa structures adopted in this work (device A) and in our previous work (device B) [8]. For clarity, note that Figure 1 is not drawn to scale and that both devices share the same epi-layer structures. The inset of Figure 1 represents the top view of the fabricated device with an active mesa diameter of 240 µm. The diameter of the active optical window is 200 µm. Such a large optical window diameter aids in collecting weak reflected light in our well established FMCW lidar system, which will be discussed in detail later. From top to bottom, the structure of both devices is composed of a p+-$In_{0.53}Ga_{0.47}As$ contact layer, p+-$In_{0.52}Al_{0.48}As$ window layer, intrinsic $In_{0.53}Ga_{0.47}As$ absorbing layer, two p-type $In_{0.52}Al_{0.48}As$ charge (field control) layers, and two intrinsic $In_{0.52}Al_{0.48}As$ multiplication layers and N+ $In_{0.52}Al_{0.48}As$ /InP contact layers. Two $In_{0.52}Al_xGa_{0.48-x}As$ graded bandgap layers are inserted at the interfaces between the absorber/window and absorber/multiplication layers, respectively. The thickness of each epi-layer is stated clearly in the figure. In order to facilitate a stepped electric field profile, the 500 nm thick multiplication (M-) layer is subdivided into two parts of 200 nm and 300 nm using additional charge control layer, as shown [10,11]. The electric field distribution within the device is simulated by using the Silvaco Technology Computer Aided Design (TCAD) tools[1]. Figure 2 (a) shows the calculated electric fields for our demonstrated APD along the vertical direction (AA') at the punch-through (V_{pt}) and breakdown voltage (V_{br}). As can be seen, even under V_{br} operation, the E-field in the $In_{0.53}Ga_{0.47}As$ layer is well below its critical field (~150 kV/cm [12]). In addition, due to the stepped electric (E-) field profile in the multiplication region, the electrons are energized in the first M-layer with a thickness of 200 nm. Due to the insufficient electric field strength in this region, the electrons are unable to trigger significant impact ionization. Eventually, the electrons transit to the second 300 nm thick M-layer for the initiation of successive impact ionization. Moreover, this dual M-layer design provides better localization of impact ionization than can be achieved in a single uniform 500 nm thick M-layer and therefore it can significantly reduce the delay time induced by the avalanche process in the APD. Furthermore, the hole impact ionizations are suppressed due to the lower and lower E-field they encounter as they travel back toward the absorption layer, which may also reduce the excess noise (k-factor) of APD. In addition, the cascade avalanche process in the demonstrated dual M-layer structure avoids pushing the single M-layer into the deep avalanche regime under the desired high-gain operation. Overall, a shorter avalanche delay time, a lower excess noise (k-) factor, and a larger GBP than those obtainable with the traditional APD design with the same M-layer thickness can thus be expected in our dual M-layer design.

Compared to device B with triple mesas, device A with the quadruple mesa structure provides better E-field confinement at the edge of the M-layer of the bottommost mesa. This is because the additional second mesa in device A, which is etched through the first field control (charge) layer and stops at first M-layer, can more effectively constrain the E-field below it [10,11]. Figures 2 (b) and (c) show the calculated electric fields of devices A and B along the horizontal directions at the first (BB') and second (CC') M-layers under a breakdown voltage of (-51 V). We can clearly see, as expected, that the electric field reduces from 750 to 90 kV/cm at the sidewall of the second M-layer in device A. Consequently, there is a reduction in the leakage current, better E-field confinement and hence suppression of the edge breakdown in our proposed APD structure.

III. MEASUREMENT RESULTS

Figures 3 (a) and (b) show the measured bias-dependent dark current, photocurrent, and operation gain of devices A and B, respectively, subjected to different optical pumping powers at an optical wavelength of 1.55 µm. The measured breakdown voltage (V_{br}) and punch through voltage (V_{pt}) of device A (B) are around -51 (-43.2) and -24 V, respectively. As can be seen, the values of V_{pt} are the same for both devices but device A exhibits a lower leakage current and larger V_{br}. These results suggest that the overall doping in the charge layers of devices A and B is pretty close and the

[1]Silvaco, 2811 Mission College Boulevard, 6th floor, Santa Clara, CA 95054

This article has been accepted for publication in a future issue of this journal, but has not been fully edited. Content may change prior to final publication. Citation information: DOI 10.1109/ACCESS.2021.3089082, IEEE Access

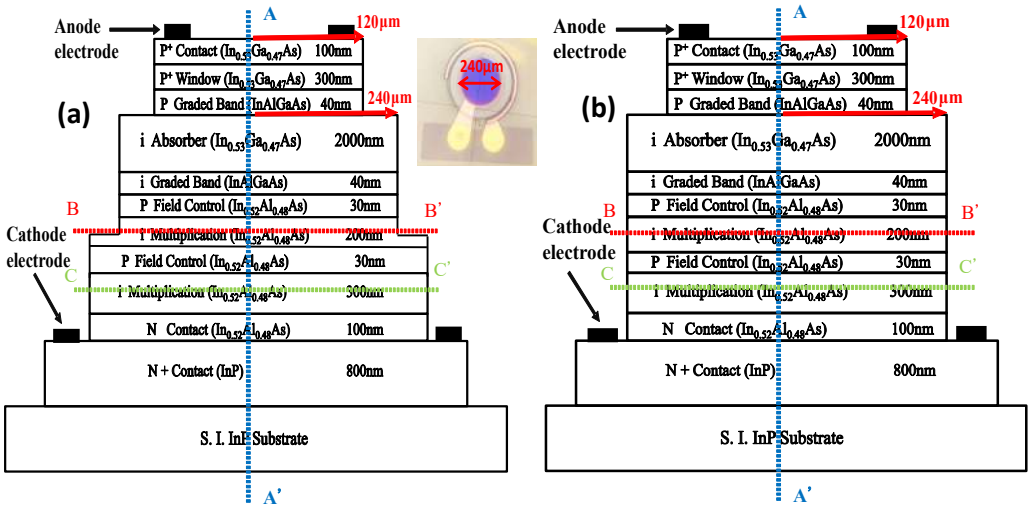

FIGURE 1. Conceptual cross-sectional view of the demonstrated APDs (a) quadruple mesa structure (Device A) (b) triple mesa structure (Device B). Inset shows the top view with an active mesa radius of 120μm in both cases.

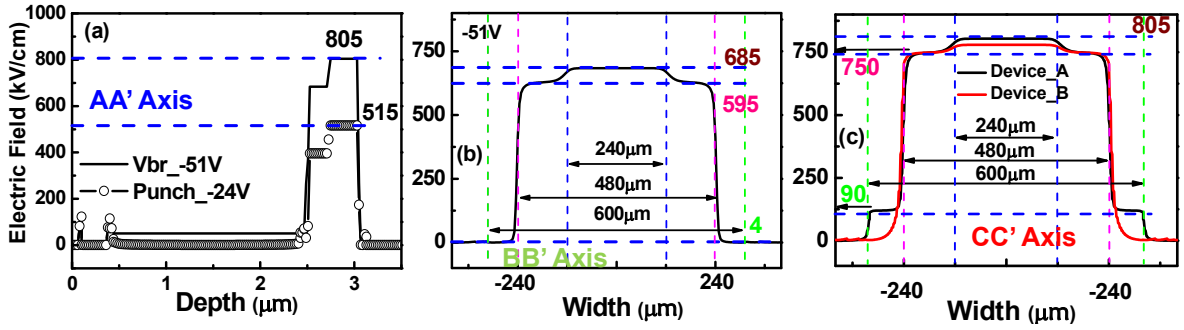

FIGURE 2. Electric field profiles at V_{pt} and V_{br} along the direction (a) AA' for device A (b) BB' for device A and (c) CC' for devices A and B, respectively.

larger V_{br} with less dark current in device A can be attributed to suppression of the edge breakdown phenomena due to its quadruple mesa structure as discussed above. With a 2 μm-thick $In_{0.53}Ga_{0.47}As$ absorption layer, the theoretical maximum unit gain responsivity will be around 1 A/W at the 1.55 μm wavelength. Here, the photo-absorption constant used for the $In_{0.53}Ga_{0.47}As$ layer at this wavelength is around 0.8 μm^{-1} [13] and we assume zero-coupling loss and single-pass light injection into the absorption layer for our device. The gain versus bias voltages under different optical pumping powers (1 to 240 μW) are also provided in the figures for reference. As can be seen, there is a significant reduction in the measured operation gains once the reverse bias voltage is above V_{br}. This can be attributed to the tremendous increase in the dark current, which then dominates over the photocurrent in the total measured current (i.e., sum total of photocurrent and dark current). In addition, we can clearly observe the gradual decrease in the maximum operation gain with the increase in the pumping power. This phenomenon can be explained by the space charge screening (SCS) effect induced by the photo-generated holes in the thick and undoped $In_{0.53}Ga_{0.47}As$ absorption layer, which reduces the net E-field and multiplication gain in the M-layer [11].

Figures 4 and 5 shows the bias-dependent O-E frequency responses of device A measured under low (1 μW) and high (100 and 240 μW) optical pumping powers at a wavelength of 1.55 μm, respectively. Under a low (1 μW) optical pumping power, we can clearly see the unvarying value (~1.22 GHz) in the measured 3-dB O-E bandwidths with the increase in the reverse bias voltage (operation gain). Only a minute degradation in bandwidth (from 1.22 to 1.16 GHz) can be observed at -49 V bias voltage, which is close to V_{br}. This phenomenon conflicts with the phenomenon reported for most of the APDs, which usually exhibit a serious degradation in the O-E bandwidth with an increase in the operation gain due to the increase in the avalanche induced delay time with the gain. Thus, the trade-off between the operation gain and the speed can be fundamentally overcome because of the cascade avalanche processes in our dual M-layer design, as discussed above. Similarly, under a high optical pumping power, as shown in Figure 5, the measured 3-dB O-E bandwidths of device A are pinned at around 1.2 GHz, regardless of the changes in the reverse bias voltages. These bandwidth values are close to the maximum O-E bandwidths of the device measured under low power excitation, as shown in Figure 4. Such invariant high-speed performance can be attributed to a significant

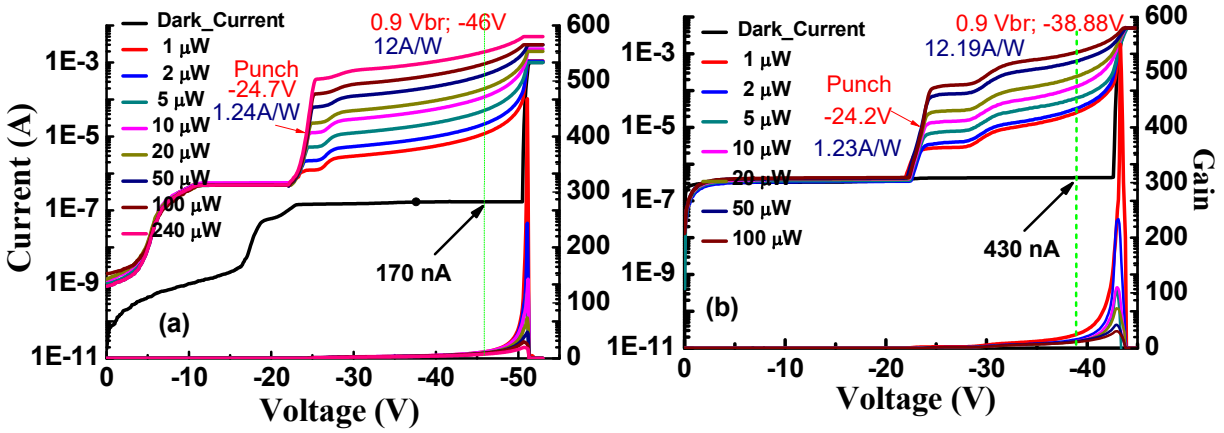

FIGURE 3. The measured dark current, photocurrent, and operation gain versus bias voltages under different optical pumping powers for the demonstrated APD operating at a wavelength of 1.55 μm for (a) Device A and (b) Device B, respectively.

reduction in the values of the operation gain, which becomes much less sensitive to the reverse bias voltage under high-power operation, as shown in Figure 3. The delay time induced by the avalanche gain, which is the major bandwidth limiting factor of an APD under high-gain (high-bias) operation is thus minimized, resulting in the invariance 3-dB O-E bandwidth [11].

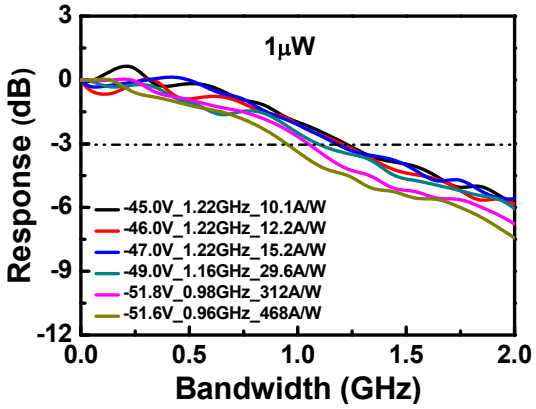

FIGURE 4. The measured bias dependent O-E frequency responses of device A under a 1 μW optical pumping power at the 1.55 μm wavelength.

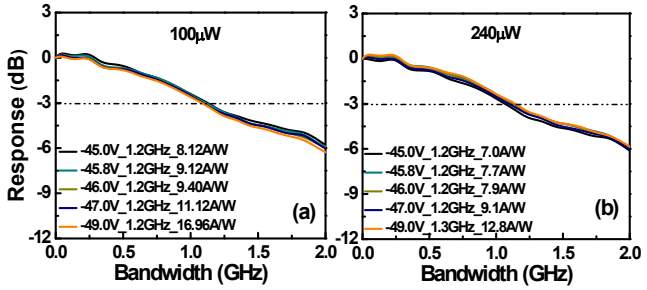

FIGURE 5 The measured bias dependent O-E frequency responses of device A under (a) 100 μW and (b) 240 μW optical pumping power at the 1.55 μm wavelength.

Figure 6 shows the 3-dB O-E bandwidths versus operation gains of devices A and B measured under a low (1 μW) optical input power. As can be seen, both devices have similar bandwidth performance under low gain operation (<100). On the other hand, when the operation gain increases further, device A exhibits a slightly larger bandwidth and gain-bandwidth product (GBP) performance than those of device B (450 vs. 432 GHz). This can be attributed to that the fact that the edge breakdown phenomenon under extremely high gain operation has been well suppressed in device A with its quadruple mesa structure, as illustrated in Figure 3. In addition, the achieved high GB product (450 GHz) can be attributed to the cascade avalanche process in the dual M-layers design, as discussed earlier. Furthermore, compared to the gain-bandwidth curves of typical APDs, which usually exhibit monotonic decreases of bandwidth with an increase of the multiplication gain [14,15], our device has a good operation window. This means that a constant O-E bandwidth (~1.22 GHz) can be sustained over a wide range of operation gains (from 10 to ~300). Such consistent performance will provide significant assistance in FMCW lidar applications, which will be discussed in detail later.

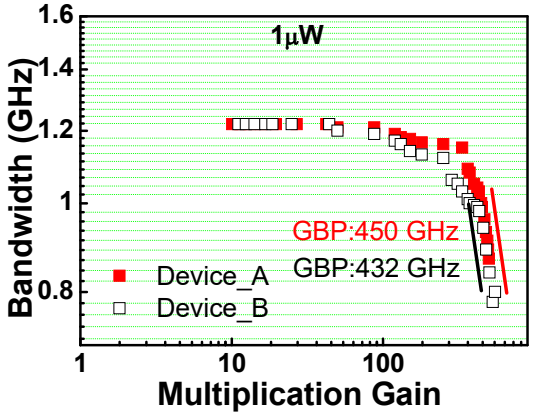

FIGURE 6 The measured 3-dB O-E bandwidths versus multiplication gain of the demonstrated APD under low (1 μW) optical pumping power for Device A and B, respectively.

IV. FMCW LIDAR SYSTEMS

We modelled a fiber based self-heterodyne FMCW lidar system using mechanical scanning mirrors [16]. As depicted in Figure 7, the modulated output light from the sweeping laser source is boosted using EDFA and further split into a signal path and a local-oscillator (LO) path using a 90/10 fiber splitter. The signal light passes through a circulator followed by a fiber collimator, producing a beam with a spot size of 0.87 mm ($1/e^2$ diameter) and a full-angle divergence angle of 0.129°. Two-dimension beam steering are achieved using two scanning galvanometer mirrors providing with a field of view of ±12.5° and a mechanical repeatability of 15 µrad (Thorlabs GVSM002-US). The light received from the target in the free space is redirected by the circulator to follow a different arm and then combined with the LO via a 50/50 fiber splitter. A variable attenuator is included in the LO path for power adjustment. The combined optical LO signal and signals reflected from the object, having a spot size of 23 µm ($1/e^2$ diameter) is fed to our demonstrated APD receiver (Rx) through a collimator followed by an aspheric lens in our FMCW lidar system. The photomixed down-converted IF signal output from the APD is then sent into an RF spectrum analyzer for analysis. The FMCW lidar system is tested using targets placed at a certain distance made from Styrofoam shaped with the letters O, F, and C. The targets are covered with retroreflective tape as shown in Figure 7. In addition to the receiver, the transmitter side also plays an important role in the FMCW lidar system. For details about our wavelength sweeping laser module the interested reader can refer to our previous work [8,17]. Under strong current modulation, the DFB laser can have significant frequency modulation (FM) due to the linewidth enhancement effect. By integrating optical limiting amplifier, the corresponding amplitude modulation is well suppressed. Figure 8 shows the output optical spectra of our wavelength sweeping laser measured under a different driving modulation signals at 1 MHz. The central wavelength of a sweeping laser under static operation (no AC driving signal) is also shown here for reference. Due to the limited resolution (~0.05 nm) of our optical spectrum analyzer (Ando AQ6315A)., the measured 3-dB linewidth (7.5 GHz) is much broader than specified for the DFB laser (~ 100 kHz). As can be seen, a higher output optical power and larger wavelength scanning ranges are obtained when the sweeping laser is modulated using a square wave signal as compared to sine and triangular modulation schemes. In addition, extremely flat-topped output optical spectra can be realized in all three modulation schemes. This result can be inferred to the efficient suppression of the residual amplitude modulation (RAM) noise during FM modulation in our sweeping laser output [18].

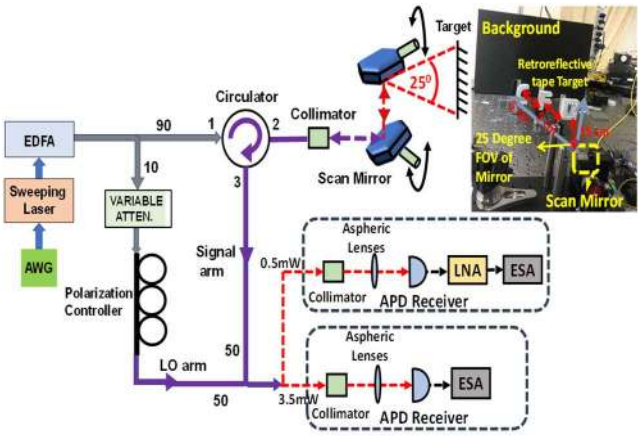

FIGURE 7 **Conceptual diagram of our established FMCW lidar system with APD Rx (Device A). FG: function generator. EDFA: erbium-doped fiber amplifier. ESA: electrical spectrum analyzer. Solid line: optical path along the fiber. Dashed line: optical path in free space.**

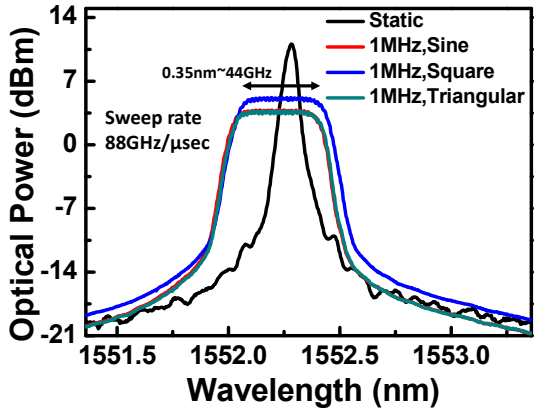

FIGURE 8 **The measured optical spectra of our sweeping laser under different modulation signals.**

V. FMCW LIDAR MEASUREMENT RESULTS

Figure 9 shows the self-heterodyne beating intermediate frequency (IF) versus different delay line distances (time) at the driving conditions (square waveform) specified in the figures for our sweeping laser source. The inset shows the corresponding output IF spectra for device A. The delay line length is achieved by changing the distance between the OUT and the scanning mirror. The IF frequency in an FMCW lidar system is determined by taking the product of the frequency ramp rate and the delay time. As can be seen, a linear relation between the delay time (distance) and the beating frequency can be obtained, which is a pre-requisite for a high-performance FMCW lidar system. The distance information can be determined from the slope of these traces and the measured IF frequency of the OUT, which will be discussed in detail later. In order to optimize the modulation condition of our sweeping laser in the established FMCW lidar systems, we measured the signal-to-noise ratio (SNR) of the down-converted IF signal output from device A using the above setup.

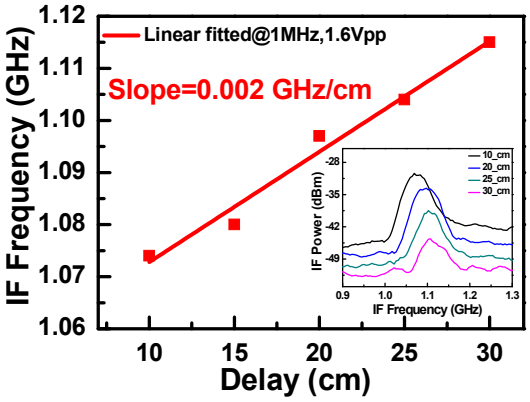

FIGURE 9 The IF beating frequency versus different delay line distances for the optimized driving conditions (1MHz, 1.6 Vpp, Square) on the sweeping laser. The inset shows picture of the corresponding IF spectra for different delays.

Figure 10 shows the measured SNR versus received optical power of device A obtained under a fixed optimized reverse dc bias of -46 V (0.9 V_{br}) and at different modulation schemes (Sine, Triangular and Square) of wavelength sweeping laser. Here, the SNR is defined by the difference in power levels between the peak of the IF tone and its corresponding noise floor. The received optical power represents the optical power measured at the 3rd port of the circulator, as shown in Figure 7. Compared to the SNR measurements reported in our previous work [8], here, the low-noise RF amplifier (LNA), which is integrated with the output of APD, has been removed. A strong optical LO signal is adopted to maximize the magnitude of the IF signal output from the APD directly without using any electrical amplifier. As can be seen, when the optical LO power is increased from 2 to 3.5 mW under square wave modulation, there is no significant enhancement in the IF signal. This indicates that the optimum LO power for FMCW lidar image is around 3 mW. Furthermore, compared with sweeping laser under sinusoidal and triangle modulation schemes, square waveform modulation provides a more significant IF peak and better SNR throughout the whole range of received optical powers (0.1 to 100 μW). Figures 11 (a) and (b) show the corresponding IF spectra for device A obtained under a fixed optical LO pumping power and different received powers under square and sinusoidal waveform modulation, respectively. We can clearly see that, in contrast to the triangle waveform modulation, the square waveform one shows a more significant IF tone with a larger SNR.

Figure 12 shows the measured dc output photocurrent versus the input optical power for device A. As can be seen, when the launched optical power is close to the optimum LO power (around 2 mW), as discussed above, the output photocurrent does not show significant saturation and it can reach 12.7 mA at a bias of 0.9 V_{br}. The corresponding responsivity under such a high output current can be as high as 6.3 A/W. Such a high responsivity under high output photocurrents facilitates the utilization of our demonstrated APD in a self-heterodyne FMCW lidar system allowing a larger S/N ratio and a lower optical power budget than those of the traditional p-i-n PD based receivers.

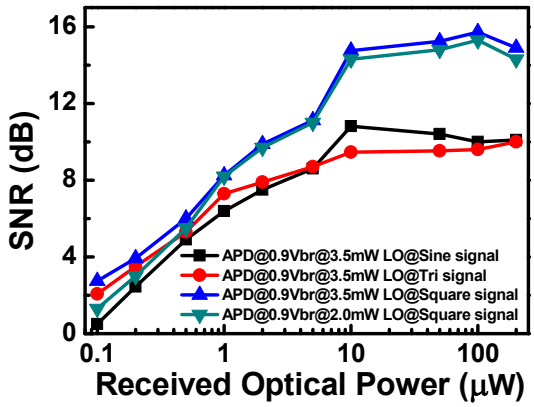

FIGURE 10 The measured SNR vs. received optical power under different optical LO pumping powers on device A at the optimized driving conditions (1MHz, 1.6 Vpp, Square) on the sweeping laser. The APD bias is fixed at 0.9Vbr.

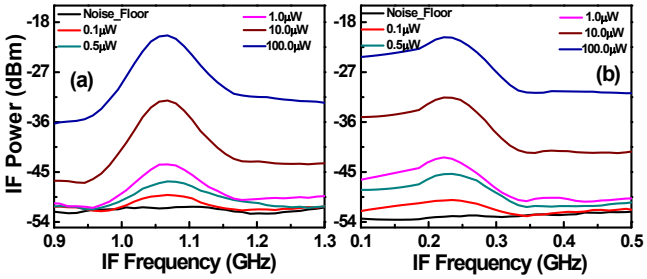

FIGURE 11 The measured IF spectra of the received optical power at a fixed 3.5mw LO power for device A at 0.9 Vbr bias at the optimized driving conditions (1MHz, 1.6 Vpp, Square) on the sweeping laser under (a) square modulation and (b) triangle modulation signals, respectively.

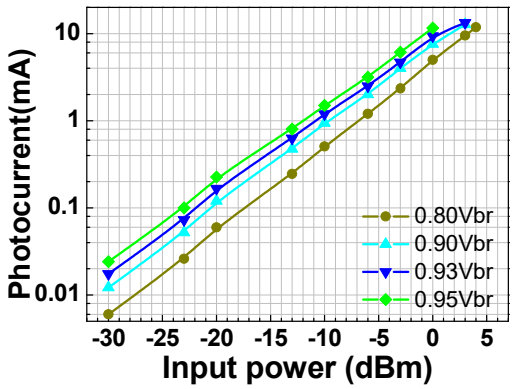

FIGURE 12 The measured DC output photocurrent versus input optical input power for device A at 1.5μm wavelength.

Figure 13 (a) shows the measured photo-generated RF power at 1 GHz versus the output photocurrent of device A with the bias fixed at 0.9 V_{br} (-46 V) in the self-heterodyne beating setup, as illustrated in Figure 7. Here, the wavelength

sweeping laser is modulated by the square waveform. The ideal relation between the RF power and averaged photocurrent obtained with a 100% optical modulation depth under a 50 Ω load is plotted for reference. We can clearly see that the output power from device A is around 6 dB larger than that of the ideal line under the same output photocurrent, which indicates that our sweeping wavelength laser source can provide an effective optical modulation depth of up to 200 %. Moreover, the maximum output power of device A can be as high as +6.95 dBm at an output photocurrent of around 7 mA, which is limited by thermal failure of the device. As compared to our previous work [9], due to further optimization of the sweeping laser driving conditions, there is an approximately 2.5 dB improvement in the maximum photo-generated RF power (6.95 vs. 4.5 dBm) obtained in this work at a higher self-heterodyne beating frequency (1 vs. 0.6 GHz). The measured photo-generated RF power at 0.5 GHz versus output photocurrent of a commercially available p-i-n PD module, which has a built-in 50 Ω load (Newport 1623)[1], is also shown in this figure for comparison. This p-i-n PD is powered by a 9V DC battery and has a ball lens in its optical window to collect the free-space input light efficiently. It has a responsivity of 1 A/W, which is the same as the unit gain responsivity of our demonstrated APDs, with a 3-dB O-E bandwidth at around 0.6 GHz. Due to the integrated 50 Ω load inside the module, its effective load resistance thus becomes 25 Ω. The 25 Ω ideal line of photo-generated RF power is also given in this figure for reference. We can clearly see that our demonstrated APD can have a much larger maximum RF power (+6.95 vs. -3.5 dBm) and higher responsivity (6.3 vs. 1 A/W), and a close value for the saturation current (~8 mA). These improvements clearly show the advantages of using our APDs for FMCW lidar application.

Figure 13 (b) represents the comparison of the photo-generated RF output power obtained using the self-heterodyne and heterodyne beating set-up at the same beating frequency of 1 GHz and different V_{br}. Here, our heterodyne-beating system is composed of two free-running lasers operated at an optical wavelength of around 1.55 μm with a 1 GHz (0.008 nm) spacing in their central wavelengths. Compared with the heterodyne-beating setup, we can clearly see that under the same output photocurrent, we can obtain significant improvements (as large as 9 dB) in the output RF power and the effective optical modulation depth (~70 to 200 %) using self-heterodyne beating setup. This advantage will in turn lead to less optical LO power being required, thus effectively increasing the power budget in the FMCW lidar system. This tremendous increase in the optical modulation depth can be attributed to the distortion of the generated sinusoidal optical waveform from our sweeping laser source under large-signal driving (1.6 V_{pp}), which leads to the optical pulse like waveform. Photo-generated microwave and millimeter-wave powers with over 100% optical modulation depths have been reported through the use of the optical pulse shaper [19], semiconductor mode-locked laser [20], and electro-optical (E-O) modulator under class AB operations [21]. In order to precisely characterize the optical waveform generated from our self-heterodyne beating system, a fast optical receiver (PT-40D/8XLMD)[2] connected with a real-time scope (MSO 72504DX)[3], which can provide a less than 10 ps time resolution, is adopted to measure the generated optical waveform.

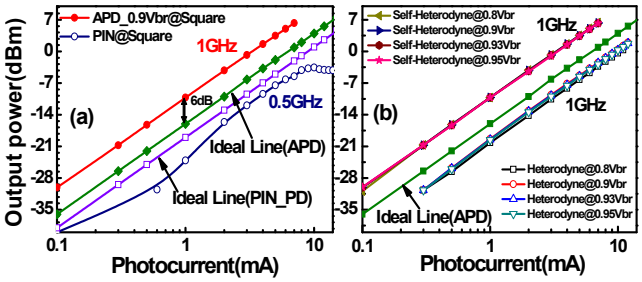

FIGURE 13 The photo generated IF power from device A versus photocurrent at the optimized driving conditions (1MHz, 1.6 Vpp, Square) on the sweeping laser obtained (a) using the self-heterodyne beating set-up at a fixed bias 0.9Vbr under square modulation and (b) comparison using heterodyne and self-heterodyne beating schemes under square modulation, respectively.

Figure 14 (a) and (b) shows the captured time-domain waveform and the corresponding fast Fourier transform (FFT) spectrum of optical pulse train, respectively. As can be seen, the distorted sinusoidal waveform behaves like an optical pulse train with a full-width half maximum (FWHM) pulse-width of 0.3 ns and a pulse repetition rate (PRR) of 1 ns. The obtained pulse like waveform thus results in the observed high (>100%) optical modulation depth. In addition, the harmonics (> 1 GHz) in the FFT spectrum should have no significant influence on our FMCW lidar system due to the limited O-E bandwidth of APD at around 1 GHz.

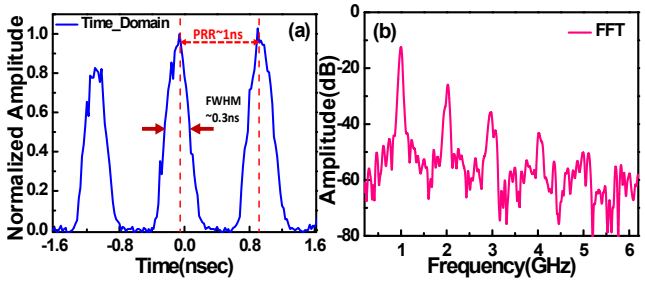

FIGURE 14 Time domain analysis representation with FWHM of 0.3nsec and PRR of 1nsec and (b) FFT representation of the down converted IF frequency.

Figure 15 shows the images of the OUTs (O, F, and C) captured using our demonstrated APD (device A) with and without the integration of a RF low-noise-amplifier (LNA) serving at the receiver-end in our well established self-

[1]Newport Corporation, 1791 Deere Avenue, Irvine, CA, 92606.

[2]Picometrix, LLC. 2925 Boardwalk, Ann Arbor, MI, 48014.

[3]Tektronix, Inc. 14150 SW Karl Braun Drive, P.O. Box 500 Beaverton, OR 97077, US.

heterodyne based FMCW lidar system. These images are constructed based on the down-converted IF frequencies and power in each pixel. The measurements setups are shown in Figures 7. Here, the free space output optical power from the scanning mirror is around 20 mW and the captured optical power reflected from the OUTs into port 3 of the circulator is in μW levels. The values of the optical LO pumping power and bias voltages applied to the APDs have been optimized according to the measurement results, as shown in Figure 10. The modulation conditions (amplitude and frequency of square wave for laser driving) of the wavelength sweeping laser have been adjusted to keep the IF down-converted signal (~1 GHz) within the bandwidth limitations of our APD (1 GHz). For the case where an APD is integrated with RF LNA, there is a reduction in the optical LO power from 3.5 to 0.5 mW for the optimized S/N ratio [8]. As can be seen in Figures 15 (a), by increasing the optical LO pumping to 3.5 mW, a clear 2-D image can be constructed without the use of an additional electrical amplifier (LNA). Such a good performance can be attributed to the excellent high-power performance of the APD as discussed above. On the other hand, as shown in Figure 15 (b), although the OUT images captured using the APD with the integrated LNA are of better quality than those obtained without one, this is at the expense of increased cost and size of the whole lidar system. Moreover, a better signal-to-noise (S/N) ratio in the captured images can be expected by further increasing the optical power of the sweeping laser source instead of using an additional EDFA, as is the case for our demonstrated system here.

The depth information of these targets can be directly evaluated using the slopes of the IF frequency versus delay distance (as illustrated in Figure 9) and the difference in the IF frequency between the pixels of the targets. Figures 15 (c) and (d) shows the 3D images with depth and IF frequency information obtained using the APD (device A) based Rx without and with the LNA, respectively. We can clearly see that the round trip lidar distances measured from the emitting aperture to the "O", "F" and "C" targets are around 30, 40 and 50 cm, respectively. These values be the same as the real distances between these three targets as shown in Figure 7.

Figure 16 represents the typical measured IF spectra of pixels from the targets (O, F, and C) and the backgrounds. Here, the background signal is induced by parasitic reflections between port 3 of the circulator and the coupling optics (collimators or fiber connectors) used for feeding the light onto the APD Rx. It is evident that the APD without LNA based Rx can provide a narrower linewidth of IF signal, consequently, better depth information can be expected. This phenomenon may be attributed to that the extra electrical phase noise induced by the LNA.

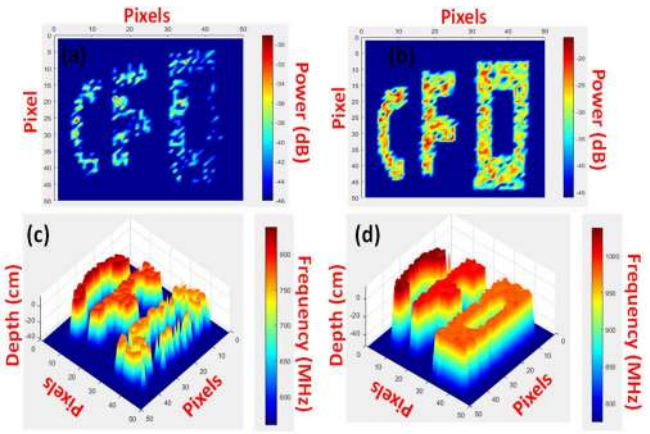

FIGURE 15 **The captured lidar images based on the measured IF power of each pixel from the (a) APD without LNA and (b) APD with LNA. The captured lidar 3D images based on the measured IF frequency and depth information of each pixel from the (c) APD without LNA (d) APD with LNA, respectively.**

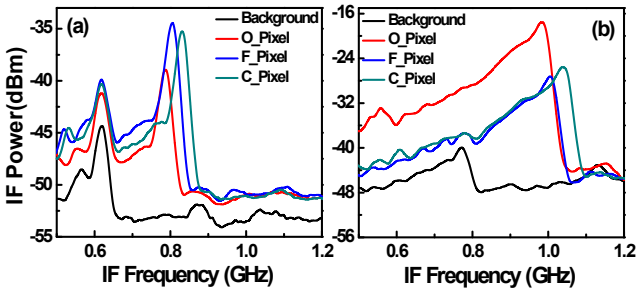

FIGURE 16 **The captured IF spectra of a single pixel from the background and the O, F and C shaped targets obtained under the square modulation setup using the (a) APD without LNA and (b) APD with LNA, respectively.**

VI. CONCLUSION

In conclusion, we demonstrate novel top-illuminated APD structures with excellent high-power and high-responsivity performance for self-heterodyne FMCW lidar applications. By implementing dual M-layer design with special mesa structures to suppress edge breakdown, such APDs can fundamentally relax the trade-off between the multiplication gain and the speed thereby facilitating higher saturation power performance. Under low power excitation (1 μW), our demonstrated APDs with a high unit gain responsivity (1 A/W) can sustain an invariable speed performance (~1.22 GHz 3-dB bandwidth) over a wide range of operation gains (1 to 400). On the other hand, as compared to the reference p-i-n PD module under high-power operation, our APD demonstrates a much larger maximum RF power (+6.95 vs. -3.5 dBm), higher responsivity (6.3 vs. 1 A/W), and a close value of saturation current (~8 mA) in our self-heterodyne based lidar system. Where, we modulate the sweeping laser source with the square waveform signal to introduce distortion, which generates pulse like

waveforms, thus hence providing an effective optical modulation depth up to 200%. Due to the excellent performance of our APD device and light sources, high-quality 3-D lidar image can be obtained without requiring the use of an electrical amplifier at the receiver-end.

REFERENCES AND LINKS

[1] Jin-Wei Shi, Jiun-In Guo, Manabu Kagami, Paul Suni, and Olaf Ziemann, "Photonic technologies for autonomous cars: feature introduction," *Optics Express,* vol. 27, pp. 7627-7628, March, 2019.

[2] B. Behroozpour, P. A. M. Sandborn, N. Quack, T. J. Seok, Y. Matsui, Ming C. Wu, B. E. Boser, "Chip-Scale Electro-Optical 3D FMCW Lidar with 8μm Ranging Precision," *ISSCC Dig. Tech. Papers,* San Francisco, CA, USA, pp. 214-215, Feb. 2016.

[3] J. Hecht, "Lasers for Lidar: FMCW lidar: An alternative for self-driving cars," *Laser Focus World,* (2019). [online] Available: https://www.laserfocusworld.com/home/article/16556322/lasers-for-lidar-fmcw-lidar-an-alternative-for-selfdriving-cars

[4] Y. Li and J. Ibanez-Guzman, "Lidar for Autonomous Driving: The Principles, Challenges, and Trends for Automotive Lidar and Perception Systems," in *IEEE Signal Processing Magazine,* vol. 37, no. 4, pp. 50-61, July 2020, doi: 10.1109/MSP.2020.2973615.

[5] P. Adany, C. Allen, and R. Hui, "Chirped Lidar Using Simplified Homodyne Detection," *J. Lightwave Technol.* vol., 27, pp. 3351-3357, Aug., 2009.

[6] M. Nada, Y. Yamada, and H. Matsuzaki, "A High-Linearity Avalanche Photodiodes with a Dual-Carrier Injection Structure," *IEEE Photon. Technol. Lett,* vol. 29, pp. 1828-1831, Nov., 2017.

[7] P. Runge, G. Zhou, T. Beckerwerth, F. Ganzer, S. Keyvaninia, S. Seifert, W. Ebert, S. Mutschall, A. Seeger, and M. Schell, "Waveguide Integrated Balanced Photodetectors for Coherent Receivers," *IEEE Journal of Selected Topics in Quantum Electronics*, vol. 24, no. 2, pp. 1-7, March-April 2018.

[8] Z. Ahmad, Sheng-I Kuo, You-Chia Chang, Rui-Lin Chao, Naseem, Yi-Shan Lee, Yung-Jr Hung, Huang-Ming Chen, Jyehong Chen, Chee Seong Goh, and Jin-Wei Shi "Avalanche Photodiodes with Dual Multiplication Layers and Ultra-High Responsivity-Bandwidth Products for FMCW Lidar System Applications," to be published in *IEEE Journal of Selected Topics in Quantum Electronics* 2022, doi: 10.1109/JSTQE.2021.3062637.

[9] Z. Ahmad, Y.-M. Liao, Sheng-I Kuo, You-Chia Chang, Rui-Lin Chao, Naseem, Yi-Shan Lee, and Jin-Wei Shi, "Dual M-Layers avalanche photodiode with extremely wide dynamic ranges and Ultra-High Bandwidth-Responsivity Product Performances in FMCW Lidar Systems," *Optical Fiber Communications Conference*, (*OFC'2021*), F2C.7, June, 2021.

[10] Yi-Han Chen, Jhih-Min Wun, Song-Lin Wu, Rui-Lin Chao, Jack Jia-Sheng Huang, Yu-Heng Jan, H.-S. Chen, C.-J. Ni, Hsiang-Szu Chang, Emin Chou, and Jin-Wei Shi, "Top-Illuminated $In_{0.52}Al_{0.48}As$-Based Avalanche Photodiode with Dual Charge Layers for High-Speed and Low Dark Current Performances," *IEEE J. of Sel. Topics in Quantum Electronics,* vol. 24, No. 2, pp. 3800208, March/April., 2018.

[11] Hao-Yi Zhao, Naseem, Andrew H. Jones, Rui-Lin Chao, Zohauddin Ahmad, Joe C. Campbell, and Jin-Wei Shi, "High-Speed Avalanche Photodiodes with Wide Dynamic Range Performance," *Journal of Lightwave Technology*, vol. 37, no. 23, pp. 5945-5952, 1 Dec.1, 2019.

[12] Y. L. Goh, J. S. Ng, C. H. Tan, W. K. Ng, and J. P. R. David, "Excess noise measurement in $In_{0.53}Ga_{0.47}As$," *IEEE Photon. Technol. Lett.*, vol. 17, no. 11, pp. 2412–2414, Nov., 2005.

[13] Naseem, Zohauddin Ahmad, Rui-Lin Chao, Hsiang-Szu Chang, C.-J. Ni, H.-S. Chen, Jack Jia-Sheng Huang, Emin Chou, Yu-Heng Jan, and Jin-Wei Shi, "The enhancement in speed and responsivity of uni-traveling carrier photodiodes with $GaAs_{0.5}Sb_{0.5}/In_{0.53}Ga_{0.47}As$ type-II hybrid absorbers," *Optics Express,* vol. 27, no. 11, pp. 15495-15504, May, 2019.

[14] M. Nada, Y. Yamada, and H. Matsuzaki, "Responsivity-Bandwidth Limit of Avalanche Photodiodes: Toward Further Ethernet Systems," *IEEE J. of Sel. Topics in Quantum Electronics,* vol. 24, no. 2, pp. 3800811, March/April., 2018.

[15] J. C. Campbell, S. Demiguel, F. Ma, A. Beck, X. Guo, S. Wang, X. Zheng, X. Li, J. D. Beck, M. A. Kinch, A. Huntington, L. A. Coldren, J. Decobert, and N. Tscherptner, "Recent Advances in Avalanche Photodiodes," *IEEE J. of Sel. Topics in Quantum Electronics,* vol. 10, pp. 777-787, July/Aug., 2004.

[16] Z. W. Barber, J. R. Dahl, T. L. Sharpe, and B. I. Erkmen, "Shot noise statistics and information theory of sensitivity limits in frequency-modulated continuous-wave ladar," *J. Opt. Soc. Am. A,* vol. 30, no. 7, pp. 1335, Jul. 2013.

[17] O. C. Graydon, M. N. Zervas, and R. I. Laming, "Erbium-doped-fiber optical limiting amplifiers," *J. of Lightwave Technol.*, vol. 13, pp. 732-739, May, 1995.

[18] N. Satyan, A. Vasilyev, G. Rakuljic, V. Leyva, and A. Yariv, "Precise control of broadband frequency chirps using optoelectronic feedback," *Optics Express,* vol. 17, no. 18, pp. 15991-15999, Aug., 2009.

[19] F.-M. Kuo, J.-W. Shi, H.-C. Chiang, H.-P. Chuang, H.-K. Chiou, C.-L. Pan, N.-W. Chen, H.-J. Tsai, and C.-B. Huang, "Spectral Power Enhancement in a 100-GHz Photonic Millimeter-Wave Generator Enabled by Spectral Line-by-Line Pulse Shaping," *IEEE Photonics Journal,* vol. 2, no. 5, pp. 719-727, Oct., 2010.

[20] A. Hirata, M. Harada and T. Nagatsuma, "120-GHz wireless link using photonic techniques for generation, modulation, and emission of millimeter-wave signals," *J. Lightwave Technol.*, vol. 21, no. 10, pp. 2145-2153, Oct., 2003.

[21] D. Tulchinsky, J. Boos, D. Park, P. Goetz, W. Rabinovich, and K. Williams, "High-Current Photodetectors as Efficient, Linear, and High-Power RF Output Stages," *J. Lightwave Technol.*, vol. 26, no. 4, pp. 408-416. Feb., 2008.

Zohauddin Ahmad was born in Bihar, India in 1989. He graduated from the Department of Nanoscience and Nanotechnology, Jamia Millia Islamia, New Delhi (India). He is currently pursuing a Ph.D. degree from the Department of Electrical Engineering, National Central University, Taiwan. His current research interests include high-speed modulator-based lasers, FMCW-Lidar and photonics integrated circuits.

Yan-Min Liao was born in Taoyuan, Taiwan on Feb. 24, 1997. He received his B.S degree from the Department of Electronics, Chung Yuan Christian Chung University, Taoyuan, Taiwan in 2019. He is now pursuing an M.S. degree in the Department of Electrical Engineering, National Central University, Taiwan. His current research interests include Single-Photon Avalanche diode and Avalanche Photodiode.

Sheng-I Kuo was born in Taoyuan, Taiwan on November 12, 1996. He received his B.S degree from the Department of Physics, National Chung Hsing University, Taichung, Taiwan in 2019. He is now pursuing an M.S. degree in the Institute of Electro-optical Engineering, National Chiao Tung University, under the guidance of Prof. You-Chia Chang.

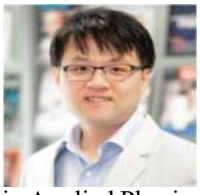

You-Chia Chang was born in Taichung, Taiwan on January 7, 1981. In 2018, he joined the Department of Photonics and Institute of Electro-Optical Engineering at National Chiao Tung University as an assistant professor. He received his Ph.D. in Applied Physics from the University of Michigan in 2016. From 2016 to 2018, he worked as a postdoctoral research scientist in the Department of Electrical Engineering at Columbia University. In 2018, he was the recipient of Jade Mountain (Yushan) Young Scholar Award. His research interests include silicon photonics, metamaterials and 2D materials.

Rui-Lin Chao was born in Taipei, Taiwan on October, 27, 1991. He received his B.S. degree from the Undergraduate Honors Program of Nano Science and Engineering, Chiao Tung University, Hsinchu, Taiwan in 2014, and now is pursuing a Ph.D. degree from the Department of Elecro-Optics, Chiao Tung University, under the guidance of Prof. Jyehong Chen, and co-advisor Prof. Jin-Wei Shi, National Central University, focusing on slow light high speed silicon based modulators, high speed photodetectors and high speed laser development and design.

Naseem was born in the Punjab, India in 1991 and completed his M. Tech at the Department of Nanotechnology, Jamia Millia Islamia, New Delhi (India). He is currently pursuing a Ph.D. degree from the Department of Electrical Engineering, National Central University, Taiwan. His current research interests include high-speed photodiodes and avalanche photodiodes for optical receivers.

Yi-Shan Lee was born in Kaohsiung, Taiwan on October 31, 1985. She is an assistant professor in the Department of Electrical Engineering, National Central University, Taoyuan, Taiwan. Her work focuses specifically on the cavity quantum electrodynamics, single photon source, entangled photon source and single photon avalanche diodes. Her recent publications can be found in Optics Letters, IEEE Photonics Technology Letters and Physical Review Letters.

Yung-Jr Hung (S'07-M'11) received his B.S. and Ph.D. degree in electrical engineering from the National Taiwan University of Science and Technology (NTUST), Taipei, Taiwan, in 2005 and 2010. He joined the faculty of the Department of Photonics, National Sun Yat-sen University (NSYSU), Kaohsiung, Taiwan in 2013 as an assistant professor and was promoted to associate professor in 2017. He joined the Department of Electrical and Computer Engineering, University of California at Santa Barbara in 2009-2010 as a visiting scholar. Dr. Hung has authored or co-authored over 100 technical journal and conference articles. He was the recipient of IEEE Best Young Professional Member Award in 2019 as well as the recipient of the MOST Da-You Wu Memorial Award in 2020. His current research interests are in the area of CMOS-compatible optoelectronic devices.

Huang-Ming (Philip) Chen received the Ph.D. degree in material sciences from University of Rochester, Rochester, New York, USA, in 2003. He joined the Faculty of the Department of Photonic and Institute of Display, National Chiao Tung University, Hsinchu, Taiwan, after postdoctoral research in 2004. His current research is focused on fast switch liquid crystal photonic devices, gas sensors, and ink-jet printing technology for flexible electronics. He is a current member of the Society of Information Display, International Liquid Crystal Society, and American Chemical Society.

Jason (Jyehong) Chen received his BS and MS degree in Electrical Engineering from National Taiwan University, Taiwan, in 1988 and 1990 respectively and the Ph.D. degree in Electrical Engineering and Computer Science from University of Maryland Baltimore County, Maryland, USA, in 1998. He joined JDSU in 1998 as senior engineer and obtained 15U.S. patents. He joined the faculty of National Chiao-Tung University, Taiwan, 2003, where he is currently a professor and chairman of the department of photonics. Prof. Chen published more than 100 papers on international journals and conferences and has been invited to give invited talks at numerous technical conferences including OFC, Photonic West, and ECOC. His research interests focus on hybrid access network, long reach passive optical networks and optical interconnects.

Jin-Wei Shi (M'03–SM'12) was born in Kaohsiung, Taiwan on January 22, 1976. In 2003, he joined the Department of Electrical Engineering, National Central University, Taoyuan, Taiwan, where he has served as a professor since 2011. In 2011-2012 and 2016-2017, he joined the ECE Dept. of UCSB as a Visiting Professor. His current research interests include ultra-high speed/power photodetectors, electro-absorption modulators, THz photonic transmitters, and VCSELs. He has authored or co-authored more than 4 book chapters, 150 journal papers, 200 conference papers and holds 30 patents. In 2010 he was the recipient of the Da-You Wu Memorial Award.